Powder Technology 412 (2022) 117964

Contents lists available at ScienceDirect

Powder Technology

journal homepage: www.journals.elsevier.com/powder-technology

Short Communication

Drag force acting on ellipsoidal particles with different shape characteristics

Sadaf Maramizonouz, Sadegh Nadimi *

School of Engineering, Newcastle University, NE1 7RU, UK

HIGHLIGHTS

- The drag coefficient of ellipsoids with various shape characteristics was studied.
- The drag coefficient of CFD was compared to data of 12 known empirical drag models.
- Each model is ideal for specific particle shapes: compact, bladed, elongated, flat.
- The models by Haider and Ganser showed the highest accuracy for all the ellipsoids.

GRAPHICAL ABSTRACT

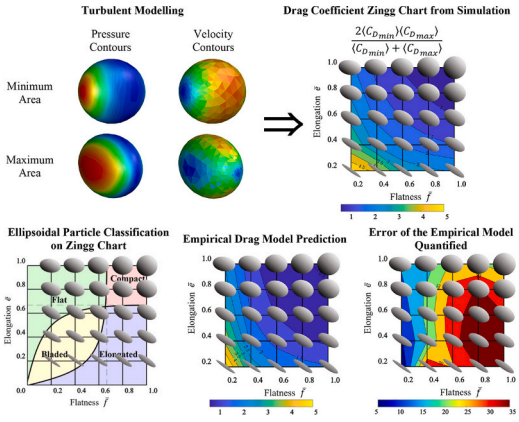

ARTICLE INFO

Keywords:
Drag force
Drag coefficient
Particle shape
Non-spherical particle

ABSTRACT

Non-spherical particles and their interaction with the surrounding fluids are omnipresent in nature and industry. While moving through fluids, particles are subjected to drag forces which is key in understating their dynamic behaviour and is highly dependent on their shape. In this research, to investigate the drag force acting on ellipsoidal particles, numerical simulations and twelve drag models are utilised to predict the particles' drag coefficients. The results are compared in a unified framework using Zingg charts. Most models compare well with the simulation results in both drag coefficient values and trends. The maximum error of these models ranges from 40% to 150%. Some models such as Haider and Levenspiel, Ganser, and Leith are capable in estimating the ellipsoids' drag coefficient with high accuracy while others either overestimate or underestimate the values. Each drag model is suitable for particles in a specific shape category including compact, bladed, elongated, or flat.

1. Introduction

Non-spherical granular materials and their interaction with the fluid around them are vastly encountered in nature. This establishes them as a significant part of various scientific fields and industries such as civil engineering, chemical engineering, powder handling, pharmaceutics, and rail industry [1,2]. Particles moving through any fluid medium

* Corresponding author.
E-mail addresses: sadaf.maramizonouz@ncl.ac.uk (S. Maramizonouz), sadegh.nadimi-shahraki@ncl.ac.uk (S. Nadimi).

https://doi.org/10.1016/j.powtec.2022.117964
Received 22 August 2022; Received in revised form 17 September 2022; Accepted 19 September 2022
Available online 23 September 2022

Nomenclature

Symbol	Name, Unit
A	Particle reference area, $[m^2]$
A_{max}	Projected area of maximum moment of inertia, $[m^2]$
A_{min}	Projected area of minimum moment of inertia, $[m^2]$
A_{mp}	Particle maximum projection area, $[m^2]$
A_p	Particle surface area, $[m^2]$
A_{sph}	Surface area of the volume equivalent sphere, $[m^2]$
C_1	Empirical parameter in some drag models, –
C_2	Empirical parameter in some drag models, –
C_3	Empirical parameter in some drag models, –
C_4	Empirical parameter in some drag models, –
C_D	Drag coefficient, –
C_{Dmax}	Drag coefficient of particle with projected area of max principal moment of inertia, –
C_{Dmin}	Drag coefficient of particle with projected area of min principal moment of inertia, –
$C_{D,\ sph}$	Drag coefficient of sphere, –
d	Particle reference length, $[m]$
d_{sph}	Diameter of the volume equivalent sphere, $[m]$
$d_{surfsph}$	Diameter of the surface area equivalent sphere, $[m]$
$\bar{e}$	Particle elongation, –
F_D	Drag force, $[N]$
F_N	Newton's formfactor, –
F_S	Stoke's formfactor, –
$\bar{f}$	Particle flatness, –
I	Intermediate dimension, $[m]$
K_N	Newton's drag correction, –
K_S	Stoke's drag correction, –
L	Longest dimension, $[m]$
P	Particle roundness, –
P_c	Perimeter of the circle equivalent to the area A_{mp}, $[m]$
P_{mp}	Maximum projection perimeter, $[m]$
R_{in}	Inradius (radius of the largest sphere which can be inscribed inside the particle), $[m]$
Re	Reynolds number, –
r	Radius of the sharpest corner, $[m]$
S	Shortest dimension, $[m]$
U	Particle velocity relative to fluid, $[m/s]$
$\forall$	Particle volume, $[m^3]$
α_2	Empirical parameter in some drag models, –
β_2	Empirical parameter in some drag models, –
μ_f	Fluid viscosity, $[N.s/m^2]$
π	Pi (ratio of a circle's circumference to its diameter), –
ρ_f	Fluid density, $[kg/m^3]$
ρ_p	Particle density, $[kg/m^3]$
Φ_C	Particle sphericity (Corey), –
Φ_K	Particle sphericity (Krumbein), –
Φ_W	Particle sphericity (Wadell), –
$\Phi_\perp$	Particle normal sphericity, –
$\Phi_\parallel$	Particle parallel sphericity, –
X	Particle circularity, –
X_{surf}	Particle surface circularity, –
Ψ	Particle shape factor, –

(such as air) experience forces and moments acting on them in various directions [3]. One of the most important forces exerted on a particle is the aerodynamic drag force. The drag force dictates the majority of the particle dynamics such as velocity and is defined as follows [3,4]:

$$F_D = \frac{1}{2}\rho_f C_D A \left|\boldsymbol{U}_p - \boldsymbol{U}_f\right| \left(\boldsymbol{U}_p - \boldsymbol{U}_f\right) \tag{1}$$

where F_D is the drag force, ρ_f is the fluid density, C_D is the particle drag coefficient, A is the particle reference area, $\boldsymbol{U}_p$ is the particle velocity, and $\boldsymbol{U}_f$ is the fluid velocity.

In the above formula, the particle drag coefficient is the most challenging to calculate [5]. For a spherical particle, C_D is a function of only the particle Reynolds number, Re, which is defined as:

$$Re = \frac{\rho_f U d}{\mu_f} \tag{2}$$

where U is the particle velocity relative to the fluid, d is the particle reference length, and μ_f is the fluid viscosity. Particle Reynolds number defines the flow regime that the particle experiences. For $Re < 3 \times 10^5$, Clift and Gauvin [6] proposed a formula to estimate C_D for spherical particles, $C_{D,\ sph}$, with excellent accuracy:

$$C_{D,sph} = \frac{24}{Re}\left(1 + 0.15Re^{0.687}\right) + \frac{0.42}{1 + \frac{42500}{Re^{1.16}}} \tag{3}$$

The drag force and how to predict it to account for the non-spherical shape of the particles are crucial in evaluating the dynamics and behaviour of non-spherical particles. There have been numerous studies on developing models to estimate the particle drag coefficient based on the shape descriptors of non-spherical particles [5,7–16]. In this research, particles' drag coefficients resulting from twelve different drag models are compared with each other and the drag coefficient resulting from numerical simulation. The data are then presented in a unified framework (using the Zingg chart [17]) to facilitate the comparison and discussions. The results stemmed from this investigation can help in tuning both Computational Fluid Dynamics (CFD) and Discrete Element Methods (DEM) by discovering and utilising the most accurate drag models.

2. Methodology

2.1. Particle shape characterisation

Characterising particles based on their physical appearance is not straightforward. Various particle shape descriptors have been proposed in the literature to measure different physical properties of the particles. However, the results of particle shape characterisation depend greatly on the chosen shape descriptors which may not necessarily be comparable to other methods [2]. Detailed discussion on the merits and drawbacks of each shape description method is beyond the scope of the current research, for more information readers are referred to the review by Blott and Pye [1] and more recent study of Angelidakis *et al* [18]. Table 1 presents some of the particle shape descriptors previously used in modelling the drag coefficient on non-spherical particles.

In the above formulas, S, I, L, and A_p can be measured by three-dimensional (3D) shape-analysis techniques and P_{mp}, $A_{mp}$by two-dimensional (2D) techniques. In other words, circularity and surface circularity are 2D descriptors and the rest are 3D.

Flatness ($\bar{f}$) and elongation ($\bar{e}$) are two of the widely used particle shape descriptors. The former conveys how plate-like a particle is while the latter is an indication of how rod-like a particle is [2]. In this research, the classification method proposed by Zingg [17] is used to present the ellipsoidal particles investigated (Fig. 1).

Table 1
Particle shape descriptors used in this study.

Shape descriptor	Formula	Description
Flatness[a]	$\bar{f} = \frac{S}{I}$	Ratio of particle's shortest dimension (S) and intermediate dimension (I)
Elongation[b]	$\bar{e} = \frac{I}{L}$	Ratio of particle's intermediate dimension (I) and longest dimension (L)
Circularity [19]	$X = P_{mp}/P_c$	Ratio of maximum projection perimeter (P_{mp}) and perimeter of the circle equivalent (P_c) to the particle maximum projection area (A_{mp})
Surface Circularity [10]	$X_{surf} = \frac{\pi d_{surfsph}}{P_{mp}}$	Ratio of perimeter of the surface area equivalent sphere ($\pi d_{surfsph}$) and maximum projection perimeter (P_{mp})
Sphericity (Wadell [20])	$\Phi_W = A_{sph}/A_p$	A measure of how spherical an object is; Ratio of surface area of the volume equivalent sphere (A_{sph}) and particle surface area (A_p)
Sphericity (Krumbein [21])	$\Phi_K = \sqrt[3]{\frac{S \times I}{L^2}}$	A measure of how spherical an object is.
Sphericity (Corey [22])	$\Phi_C = \frac{S}{\sqrt{L \times I}}$	A measure of how spherical an object is.
Normal Sphericity [9]	$\Phi_\perp$	Ratio of projected area of the volume equivalent sphere and projected area of the particle normal to the flow direction
Roundness [23]	$P = \frac{r}{R_{in}}$	A measure of how spherical an object is.
Shape Factor [24]	$\Psi = \frac{\Phi_W}{X}$	Ratio of Wadell's sphericity [20] and circularity [19]

[a] This is the original definition of flatness proposed by Zingg [24] and used in Drag models reported here. There are several definitions available in the literature please see [17] for more information.
[b] This is the original definition of elongation proposed by Zingg [24] and used in Drag models reported here. There are several definitions available in the literature please see [17] for more information.

2.2. Modelling the particles' drag coefficient

Twelve models have been chosen to evaluate the particles' drag coefficients. These models are mostly empirical and have been developed using the data extracted from various experiments. Each model uses different shape descriptors including flatness, elongation, circularity, sphericity, roundness, and shape factor. Using an initial value for the velocity, each equation for C_D can be iteratively solved to find the value for the particle drag coefficient [5,7–16]. Table 2 presents the drag models that have been used in this research.

Each of these empirical models is capable of estimating the drag coefficient through a specific range of Reynolds number. Fig. 2 presents the range of appropriate values of Reynolds number for every drag model. The area highlighted in blue shows the range of Reynolds number between 137 and 234 which is used in this study and calculated for each ellipsoidal particle based on the diameter of their volume equivalent sphere.

2.3. Numerical modelling

The computational domain for numerical modelling is three-dimensional and consists of an ellipsoidal particle placed inside a fluid domain with its geometry defined as a rectangular cuboid. The dimensions of the domain are chosen based on the work of Tagliavini *et al* [25]. The boundary conditions are defined as known velocity of 1 m/s at the inlet, known ambient pressure at the outlet, symmetry at the four sides of the rectangular cuboid and no-slip on the surface of the particle which means that the fluid velocity is zero on the particle surface due to the viscosity of the fluid. The Reynolds number for these simulations are between 137 and 234 depending on the diameter of the volume equivalent sphere for each ellipsoidal particle. The domain geometry and boundary conditions are shown in Fig. 3(a).

For each particle shape, two cases of numerical simulation have been done using first the projected area of minimum (A_{min}), and second the projected area of maximum (A_{max}) principal moments of inertia. The particle drag coefficient can be estimated with reasonable accuracy using the harmonic mean of the drag coefficients calculated using the projected areas of minimum (C_{Dmin}) and maximum (C_{Dmax}) principal moments of inertia as Tagliavini *et al* [25] had demonstrated through experiments and numerical modelling.

$$C_D = \frac{2\langle C_{Dmin}\rangle\langle C_{Dmax}\rangle}{\langle C_{Dmin}\rangle + \langle C_{Dmax}\rangle} \tag{4}$$

where $\langle \Lambda \rangle$ is the time-averaged value of the variable Λ.

For mesh dependency analysis, five different mesh resolutions with ~115,000, ~120,000, ~140,000, ~180,000, and ~240,000 tetrahedral elements were used for the computational simulations. Fig. 3(b) shows that as the mesh resolution increases the accuracy of the computational solution also increases. Increasing the mesh resolution from ~140,000 to ~180,000 results in a change of <4% in the value of the drag coefficient. So the number of elements was chosen to be ~140,000 to ensure that the computational grid is fine enough not to influence the results while also offering reasonable computational time.

In order to accurately resolve flow characteristics close to the surface of the particle, which is essential in calculating the drag force, computational mesh refinement is employed on the grid cells adjacent to the

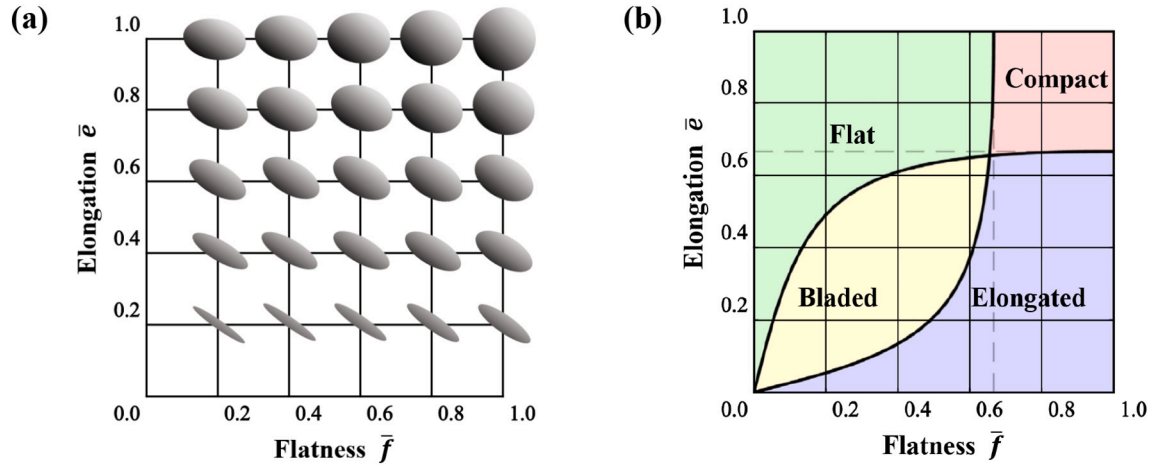

Fig. 1. (a) Ellipsoidal particle shapes with varying aspect ratios on a Zingg chart, and **(b)** The particle classification system proposed by Angelidakis et al. [18].

Table 2
Empirical drag models proposed in the literature.

Drag Model	Shape Descriptors	Drag Coefficient
Haider & Levenspiel [7]	Φ_W	$C_D = \frac{24}{Re}\left(1 + C_1 Re^{C_2}\right) + \frac{C_3}{1 + \frac{C_4}{Re}}$ $C_1 = exp\left(2.33 - 6.46\Phi_W + 2.45{\Phi_W}^2\right)$ $C_2 = 0.096 + 0.556\Phi_W$ $C_3 = exp\left(4.09 - 13.89\Phi_W + 18.42{\Phi_W}^2 - 10.26{\Phi_W}^3\right)$ $C_2 = exp\left(1.47 + 12.26\Phi_W - 20.73{\Phi_W}^2 + 15.89{\Phi_W}^3\right)$
Ganser [8]	Φ_W	$C_D = \frac{24K_S}{Re}\left(1 + 0.1118\left(\frac{ReK_N}{K_S}\right)^{0.6567}\right) + \frac{0.4305K_N}{\left(1 + \frac{3305}{\left(\frac{ReK_N}{K_S}\right)}\right)}$ $K_N = 10^{1.8148(-log\Phi_W)^{0.5743}}$ $K_S = \frac{1}{3} + \frac{2}{3\sqrt{\Phi_W}}$
Ganser [8] & Leith [9]	Φ_W $\Phi_\perp$	$C_D = \frac{24K_S}{Re}\left(1 + 0.1118\left(\frac{ReK_N}{K_S}\right)^{0.6567}\right) + \frac{0.4305K_N}{\left(1 + \frac{3305}{\left(\frac{ReK_N}{K_S}\right)}\right)}$ $K_N = 10^{1.8148(-log\Phi_W)^{0.5743}}$ $K_S = \frac{1}{3\sqrt{\Phi_\perp}} + \frac{2}{3\sqrt{\Phi_W}}$
Tran-Cong *et al* [10]	X_{surf}	$C_D = \frac{24}{Re}\left(\frac{d_{surfsph}}{d_{sph}}\right)\left(1 + \frac{0.15}{\sqrt{X_{surf}}}\left(\frac{d_{surfsph}}{d_{sph}}Re\right)^{0.687}\right) + \frac{0.42\left(\frac{d_{surfsph}}{d_{sph}}\right)^2}{\sqrt{X_{surf}}\left[1 + 42500\left(\frac{d_{surfsph}}{d_{sph}}Re\right)^{-1.16}\right]}$
Swamee & Ojha [11]	Φ_C Crushed Rock Fragments Φ_C	$C_D = \left[\frac{48.5}{\left(1 + 4.5{\Phi_C}^{0.35}\right)^{0.8} Re^{0.64}} + \left(\frac{Re}{Re + 100 + 1000\Phi_C}\right)^{0.32}\frac{1}{\left({\Phi_C}^{18} + 1.05{\Phi_C}^{0.8}\right)}\right]^{1.25}$
	Natural Sediments	$C_D = 0.84\left[\frac{33.78}{\left(1 + 4.5{\Phi_C}^{0.35}\right)^{0.7} Re^{0.56}} + \left(\frac{Re}{Re + 700 + 1000\Phi_C}\right)^{0.28}\frac{1}{\left({\Phi_C}^4 + 20{\Phi_C}^{20}\right)^{0.175}}\right]^{1.428}$
Camenen [12]	Φ_C P	$C_D = \left[\left(\frac{C_1}{Re}\right)^{1/C_3} + {C_2}^{1/C_3}\right]^{C_3}$ $C_1 = 24 + 100\left[1 - sin\left(\frac{\pi}{2}\Phi_C\right)\right]^{2.1+0.06P}$ $C_2 = 0.39 + 0.22(6 - P) + 20\left[1 - sin\left(\frac{\pi}{2}\Phi_C\right)\right]^{1.75+0.35P}$ $C_3 = (1.2 + 0.12\mathrm{P})\left[sin\left(\frac{\pi}{2}\Phi_C\right)\right]^{0.47}$ $C_D = \left[\left(\frac{C_1}{Re}\right)^{1/C_3} + {C_2}^{1/C_3}\right]^{C_3}$
Wu & Wang [13]	Φ_C	$C_1 = 53.5e^{-0.65\Phi_C}$ $C_2 = 5.65e^{-2.5\Phi_C}$ $C_3 = 0.7 + 0.9\Phi_C$
Wang *et al* [14]	Ψ	$C_D = 0.945\frac{C_{D,sph}}{\Psi^{(0.641Re^{0.153})}}Re^{-0.01}$ $C_D = \frac{24K_S}{Re}\left[1 + 0.125\left(Re\frac{K_N}{K_S}\right)^{2/3}\right] + \frac{0.46K_N}{1 + \frac{5330}{Re\frac{K_N}{K_S}}}$
Bagheri & Bonadonna [5]	$\bar{e}$ $\bar{f}$	$F_N = \bar{f}^2 \times \bar{e}\left(\frac{{d_{sph}}^3}{L \times i \times S}\right) K_N = 10^{\alpha_2(-logF_N)^{\beta_2}}$ $F_S = \bar{f} \times \bar{e}^{1.3}\left(\frac{{d_{sph}}^3}{L \times I \times S}\right) K_S = \frac{{F_S}^{1/3} + {F_S}^{-1/3}}{2}$ $\alpha_2 = 0.45 + 10/\left(exp\left(2.5log\rho_{p/\rho_f}\right) + 30\right)$ $\beta_2 = 1 - 37/\left(exp\left(3log\rho_{p/\rho_f}\right) + 100\right)$
Dioguardi & Mele [15]	Ψ	$C_D = \frac{C_{D,sph}}{Re^{2\Psi^{Re^{0.05}}}}\left(\frac{Re}{1.1883}\right)^{1/0.4826}$
Dioguardi *et al* [16]	Ψ	$C_D = \frac{24}{Re}\left(\frac{1 - \Psi}{Re} + 1\right)^{0.25} + \frac{24}{Re}\left(0.1806Re^{0.6459}\right)\Psi^{-\left(Re^{0.08}\right)} + \frac{0.4251}{1 + \frac{6880.95}{Re}\Psi^{5.05}}$

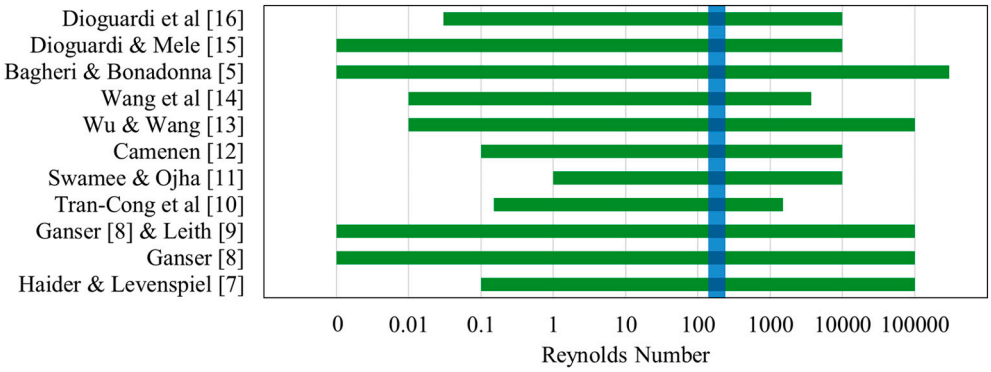

Fig. 2. Appropriate range of Reynolds number for each of the empirical drag coefficient models (shown in green) and the range of Reynolds number between 137 and 234 used in this study and calculated for each ellipsoidal particle based on the diameter of their volume equivalent sphere (shown in blue). (For interpretation of the references to colour in this figure legend, the reader is referred to the web version of this article.)

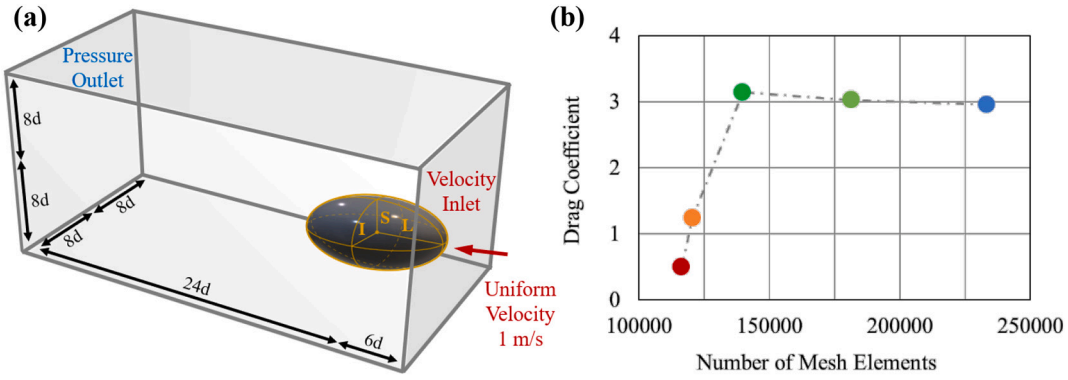

Fig. 3. **(a)** Computational domain, dimensions are a function of longest particle dimension (d = L = 0.01 m), **(b)** Mesh dependency analysis, drag coefficient versus the number of mesh elements.

particle surface. For this purpose, the thickness of the first layer is defined ~5×10^{-3} times the diameter of the volume equivalent sphere for each ellipsoidal particle. The thickness of the subsequent 29 mesh layers close to the surface of the particle grows with a ~1.2 growth rate. The size of the rest of the mesh elements gradually increases along the direction away from the particle surface with a transition ratio of ~0.3.

The governing equations of motion for the fluid are the Navier-Stokes equations in their transient form:

$$\nabla.(\boldsymbol{U}_f) = 0 \tag{5}$$

$$\rho_f\left(\frac{\partial \boldsymbol{U}_f}{\partial t} + (\boldsymbol{U}_f \bullet \nabla)\boldsymbol{U}_f\right) = -\nabla P + \mu_f(\nabla^2 \boldsymbol{U}_f) \tag{6}$$

where t is the time and P is the fluid pressure [3]. All the governing equations were discretised using the finite volume method (FVM) and were solved with the semi-implicit method for pressure-linked equations (SIMPLE) with a convergence criteria and a time step of 10^{-6}. Turbulence modelling has been performed using the Wall Adapting Local Eddy-viscosity (WALE) model [26] which based on the work of Tagliavini *et al* [25] produces the second least averaged absolute error. A total number of 54 simulations including two for each of the 25 ellipsoids and four for mesh dependency analysis have been performed using the software ANSYS FLUENT 18.1.

3. Results and discussions

3.1. Particle drag coefficient

The drag coefficients obtained from numerical simulation as well as calculated using each of the twelve drag models are plotted in Zingg charts and are shown in Fig. 4(a) to (m).

Comparing drag coefficients obtained from numerical simulation (Fig. 4(a)) to drag coefficients obtained from the twelve drag models (Fig. 4(b) to (m)), it can be seen that most models compare well with the simulation data in terms of both value and trend resulting in a maximum estimation error of between 40% to 150%. The drag coefficients calculated using the models by Haider & Levenspiel [7] (Fig. 4(b)), Ganser [8] (Fig. 4(c)), Ganser & Leith [8,9] (Fig. 4(d)), and Wang *et al* [14] (Fig. 4(j)) show the most similarity with the simulation data.

The value for the particle drag coefficient resulted from the three models proposed by Tran-Cong *et al* [10] (Fig. 4(e)), Swamee & Ojha [11] for natural sediments (Fig. 4(g)), and Dioguardi *et al* [16] (Fig. 4(m)) are overestimated especially for the particles with lower values of flatness and elongation. While the models by Swamee & Ojha [11] for crushed rock fragments (Fig. 4(f)) and Camenen [12] (Fig. 4(h)) overestimate the drag coefficient even more compared to the simulation data.

The three models presented by Wu & Wang [13] (Fig. 4(i)), Bagheri

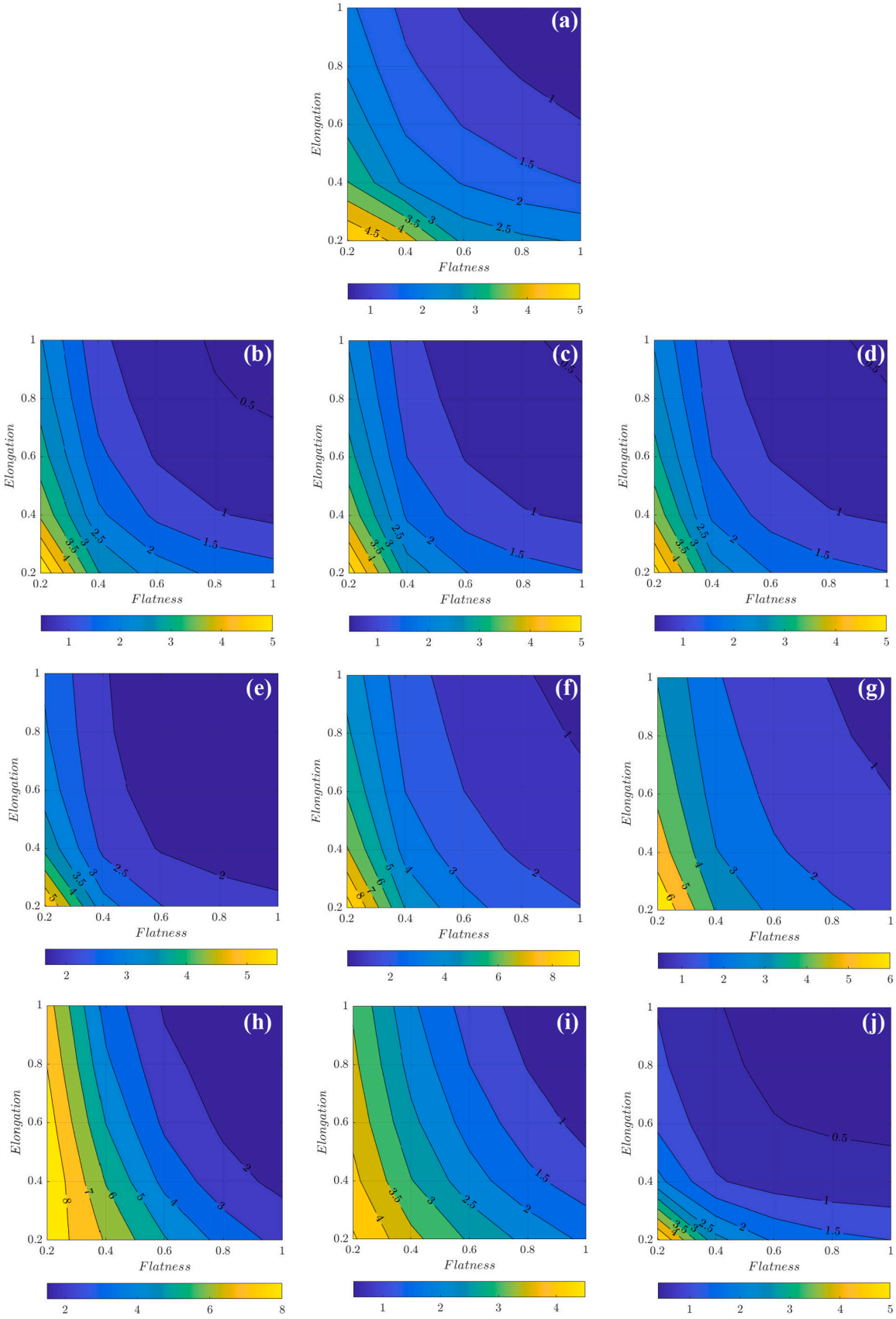

Fig. 4. Particles' drag coefficint plotted in Zingg charts obtained from **(a)** numerical simulation, **(b)** Haider & Levenspiel [7], **(c)** Ganser [8], **(d)** Ganser & Leith [8,9], **(e)** Tran-Cong et al. [10], **(f)** Swamee & Ojha (crushed rock fragments) [11], **(g)** Swamee & Ojha (natural sediments) [11], **(h)** Camenen [12], **(i)** Wu & Wang [13], **(j)** Wang et al. [14], **(k)** Bagheri & Bonadonna [5], **(l)** Dioguardi & Mele [15], and **(m)** Dioguardi et al. [16].

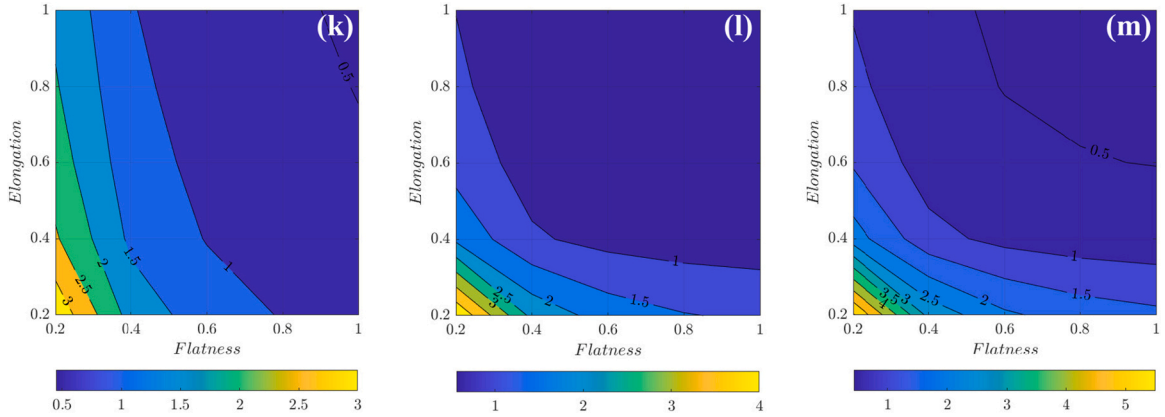

Fig. 4. (*continued*).

& Bonadonna [5] (Fig. 4(k)), and Dioguardi & Mele [15] (Fig. 4(l)) underestimate the drag coefficient especially the values which correspond to the particles with smaller flatness and elongation characteristics.

For each of the twelve drag models, the value of error compared to the data obtained from numerical simulation are plotted in Zingg charts and are shown in Fig. 5(a) to (l).

The drag coefficients obtained using the models by Haider & Levenspiel [7] (Fig. 5(a)), Ganser [8] (Fig. 5(b)), and Ganser & Leith [8,9] (Fig. 5(c)) show maximum error values of 40% or less which mostly happens for the particles with higher values of flatness. Based on the particle classification system proposed by Angelidakis *et al* [18], it is more appropriate to use these three models for flat and bladed particles.

Maximum values for the drag coefficient errors calculated from the models proposed by Wang *et al* [14] (Fig. 5(i)), Dioguardi & Mele [15] (Fig. 5(k)), and Dioguardi *et al* [16] (Fig. 5(l)) are all 60% or less and correspond to the middle area of the Zingg chart populated by the particles with intermediate flatness and elongation characteristics. These three models can be used to estimate the drag coefficient of the bladed, compact, and sometimes elongated particles.

The models presented by Swamee & Ojha [11] for natural sediments (Fig. 5(f)) and Wu & Wang [13] (Fig. 5(h)) result in a maximum error value of 60% while the models by Swamee & Ojha [11] for crushed rock fragments (Fig. 5(e)) and Camenen [12] (Fig. 5(g)) result in maximum error values of >100%. For these four models the maximum error value happens for the particles with lower values of flatness. These four models can be a reasonable choice to estimate the drag coefficient of compact, elongated and bladed particles.

Bagheri & Bonadonna's model [5] (Fig. 5(j)) shows a maximum error of 80% for particles with low elongation values. This model is more suitable for compact and flat particles. The maximum value of error resulting from using the model proposed by Tran-Cong *et al* [10] (Fig. 5 (d)) is >150% for particles with high values for both flatness and elongation making it unsuitable for spherical and compact particles.

The drag coefficient models utilised in this research can be classified in four classes based on the shape descriptor they use to estimate the particles' drag coefficient. The first group use Wadell's Sphericity (Φ_W) [20] and includes the methods by Haider & Levenspiel [7], Ganser [8], and Leith [9]. These three models are effective in a wide range of Reynolds number from 0.1 to 10^5 (for more detail see Fig. 2). With the lowest maximum error values (40% or less), these three models are shown to be suitable for all ellipsoidal particles especially the ones belonging to the flat and bladed categories.

The second group use the Shape Factor (Ψ) by Dellino et al. [24] to estimate the drag coefficient. The models by Wang *et al* [14], Dioguardi & Mele [15], and Dioguardi *et al* [16] belong to this group. These three models are operational in a wide range of Reynolds number with different lower and upper bounds (for more detail see Fig. 2). The maximum error value for this group is the second lowest (60% or less). All three models in this group are confirmed to be capable in estimating the drag coefficient of compact particles with minimum error. They may be suitable for other categories depending on the particle shape and the model chosen.

The third group use Corey's Sphericity (Φ_C) [22] and is comprised of the models by Swamee & Ojha [11], Camenen [12], and Wu & Wang [13]. These three models are functional in a smaller range of Reynolds number compared to the first two groups (for more detail see Fig. 2). The maximum error values resulting from these models range between 60% to 250% and mostly correspond to flat particles with low values of flatness. They work best for elongated particles and can be effective for some compact and bladed particles as well.

The fourth and final group utilise other shape descriptors and includes the models by Bagheri & Bonadonna [5] and Tran-Cong *et al* [10]. The former uses particles' Flatness ($\bar{f}$) and Elongation ($\bar{e}$) and is effective for the widest range of Reynolds number (for more detail see Fig. 2) and the latter uses Surface Circularity (X_{surf}) [10] and is effective for the Reynolds number between 0.15 and 1500. The model by Bagheri & Bonadonna [5] works best for compact particles (<80% error) while the one by Tran-Cong *et al* [10] can be used for all particle categories except compact which results in the maximum value of error (>150%).

4. Conclusions

In this research, the drag coefficient of ellipsoidal particles with various flatness and elongation characteristics was investigated. Numerical modelling was performed to obtain an accurate estimate of the drag coefficient and twelve different drag models were utilised to predict the particles' drag coefficients. The results from both approaches were presented on Zingg charts as a unified framework to facilitate the comparison. The data resulting from numerical simulation and drag models exhibited similar values and trends. The models presented by Haider & Levenspiel, Ganser, and Ganser & Leith were suitable for estimating the drag coefficient of ellipsoids, especially flat and bladed particles with high accuracy. Five drag models were shown to overestimate and three models were shown to underestimate the maximum value of the drag coefficient for ellipsoidal particles. For compact particles, all the models proved suitable except the one by Tran-Cong et al. For bladed and elongated particles, the models proposed by Wang *et al*, Dioguardi & Mele, Dioguardi *et al*, Swamee & Ojha, Wu & Wang, Tran-Cong *et al*, and Camenen showed promise while for flat particles, the models by Bagheri & Bonadonna and Tran-Cong *et al* proved to be efficient.

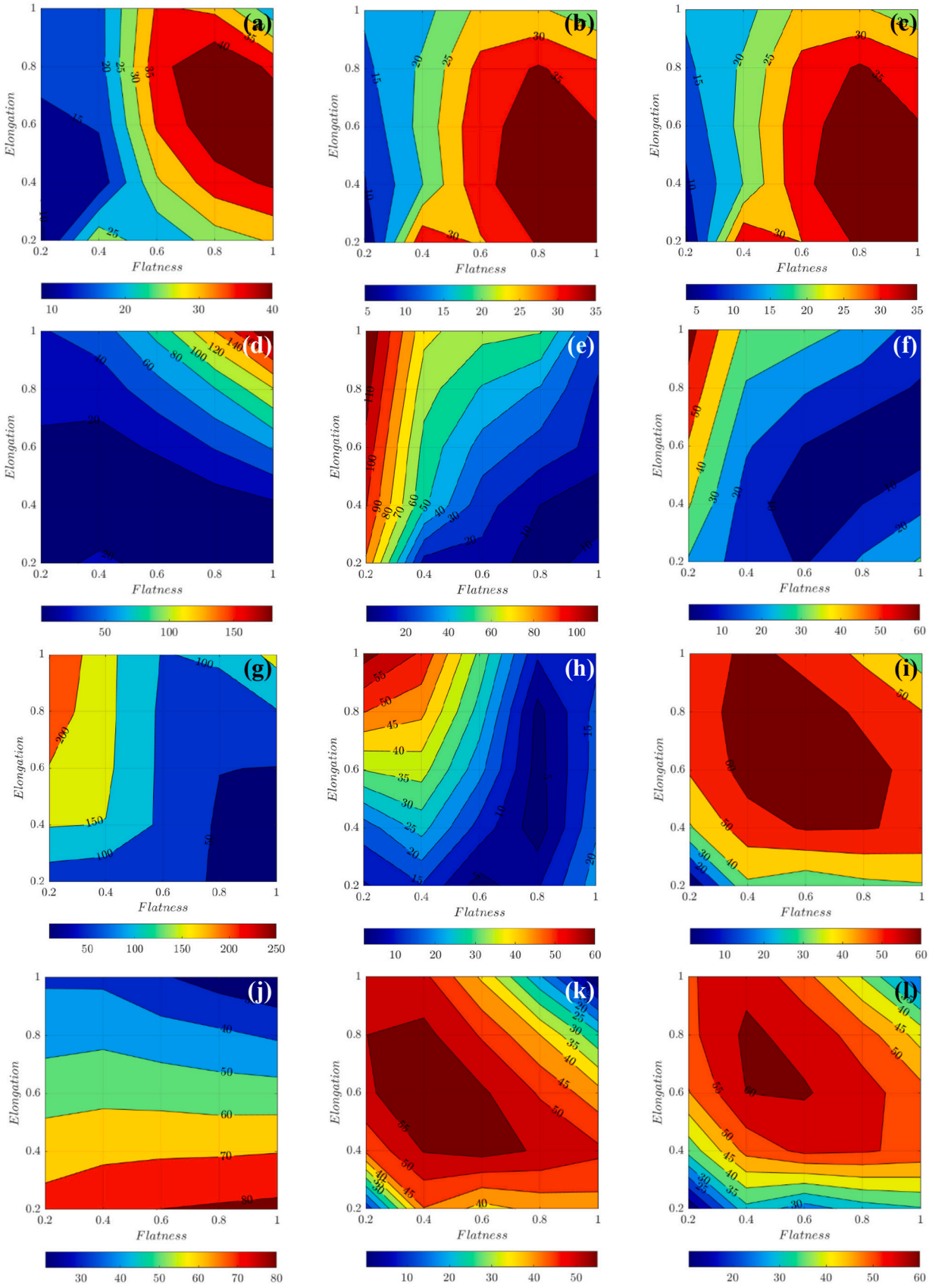

Fig. 5. Particles' drag coefficint error percentage plotted in Zingg charts obtained from comparing the numerical simulation with the model proposed by **(a)** Haider & Levenspiel [7], **(b)** Ganser [8], **(c)** Ganser & Leith [8,9], **(d)** Tran-Cong et al. [10], **(e)** Swamee & Ojha (crushed rock fragments) [11], **(f)** Swamee & Ojha (natural sediments) [11], **(g)** Camenen [12], **(h)** Wu & Wang [13], **(i)** Wang et al. [14], **(j)** Bagheri & Bonadonna [5], **(k)** Dioguardi & Mele [15], and **(l)** Dioguardi et al. [16].

CRediT authorship contribution statement

Sadaf Maramizonouz: Conceptualization, Methodology, Software, Validation, Formal analysis, Investigation, Data curation, Writing – original draft, Writing – review & editing, Visualization. **Sadegh Nadimi:** Conceptualization, Methodology, Formal analysis, Resources, Writing – review & editing, Supervision, Project administration, Funding acquisition.

Declaration of Competing Interest

The authors declare that they have no known competing financial interests or personal relationships that could have appeared to influence the work reported in this paper.

Data availability

Data will be made available on request.

Acknowledgments

This work was funded by the UK Engineering and Physical Sciences Research Council (EPSRC) grant No. EP/V053655/1 RAILSANDING - Modelling Particle Behaviour in the Wheel-Rail Interface. The authors would also acknowledge the support of Dr. Vasileios Angelidakis for plotting the Zingg charts.

References

[1] S.J. Blott, K. Pye, Particle shape: a review and new methods of characterization and classification, Sedimentology 55 (1) (2008) 31–63.
[2] V. Angelidakis, S. Nadimi, S. Utili, SHape analyser for particle engineering (SHAPE): seamless characterisation and simplification of particle morphology from imaging data, Comput. Phys. Commun. 265 (2021), 107983.
[3] F.M. White, Fluid Mechanics, Tata McGraw-Hill Education, 1979.
[4] C.T. Crowe, E.E. Michaelides, Multiphase Flow Handbook, Taylor & Francis, 2006.
[5] G. Bagheri, C. Bonadonna, On the drag of freely falling non-spherical particles, Powder Technol. 301 (2016) 526–544.
[6] R. Clift, W. Gauvin, Motion of entrained particles in gas streams, Can. J. Chem. Eng. 49 (4) (1971) 439–448.
[7] A. Haider, O. Levenspiel, Drag coefficient and terminal velocity of spherical and nonspherical particles, Powder Technol. 58 (1) (1989) 63–70.
[8] G.H. Ganser, A rational approach to drag prediction of spherical and nonspherical particles, Powder Technol. 77 (2) (1993) 143–152.
[9] D. Leith, Drag on nonspherical objects, Aerosol Sci. Technol. 6 (2) (1987) 153–161.
[10] S. Tran-Cong, M. Gay, E.E. Michaelides, Drag coefficients of irregularly shaped particles, Powder Technol. 139 (1) (2004) 21–32.
[11] P.K. Swamee, C.S.P. Ojha, Drag coefficient and fall velocity of nonspherical particles, J. Hydraul. Eng. 117 (5) (1991) 660–667.
[12] B. Camenen, Simple and general formula for the settling velocity of particles, J. Hydraul. Eng. 133 (2) (2007) 229–233.
[13] W. Wu, S.S. Wang, Formulas for sediment porosity and settling velocity, J. Hydraul. Eng. 132 (8) (2006) 858–862.
[14] Y. Wang, L. Zhou, Y. Wu, Q. Yang, New Simple correlation formula for the drag coefficient of calcareous sand particles of highly irregular shape, Powder Technol. 326 (2018) 379–392.
[15] F. Dioguardi, D. Mele, A new shape dependent drag correlation formula for non-spherical rough particles. Experiments and results, Powder Technol. 277 (2015) 222–230.
[16] F. Dioguardi, D. Mele, P. Dellino, A new one-equation model of fluid drag for irregularly shaped particles valid over a wide range of Reynolds number, J. Geophys. Res. Solid Earth 123 (1) (2018) 144–156.
[17] T. Zingg, Beitrag zur Schotteranalyse, ETH Zurich, 1935.
[18] V. Angelidakis, S. Nadimi, S. Utili, Elongation, flatness and compactness indices to characterise particle form, Powder Technol. 396 (2022) 689–695.
[19] P. Dellino, L. La Volpe, Image processing analysis in reconstructing fragmentation and transportation mechanisms of pyroclastic deposits. The case of Monte Pilato-Rocche Rosse Eruptions, Lipari (Aeolian Islands, Italy), J. Volcanol. Geotherm. Res. 71 (1) (1996) 13–29.
[20] H. Wadell, Volume, shape, and roundness of rock particles, J. Geol. 40 (5) (1932) 443–451.
[21] W.C. Krumbein, Measurement and geological significance of shape and roundness of sedimentary particles, J. Sediment. Res. 11 (2) (1941) 64–72.
[22] A.T. Corey, Influence of Shape on the Fall Velocity of Sand Grains, Colorado A & M College, 1949.
[23] C.K. Wentworth, A laboratory and field study of cobble abrasion, J. Geol. 27 (7) (1919) 507–521.
[24] P. Dellino, D. Mele, R. Bonasia, G. Braia, L. La Volpe, R. Sulpizio, The analysis of the influence of pumice shape on its terminal velocity, Geophys. Res. Lett. 32 (21) (2005).
[25] G. Tagliavini, M. McCorquodale, C. Westbrook, P. Corso, Q. Krol, M. Holzner, Drag coefficient prediction of complex-shaped snow particles falling in air beyond the stokes regime, Int. J. Multiphase Flow 140 (2021), 103652.
[26] F. Nicoud, F. Ducros, Subgrid-scale stress modelling based on the square of the velocity gradient tensor, Flow Turbulence Combust. 62 (3) (1999) 183–200.